

Ultrasensitive broadband photodetectors based on two-dimensional Bi₂O₂Te films

Pin Tian

Kunming Institute of Physics

Hongbo Wu

Beijing Institute of Technology

Libin Tang (✉ scitang@163.com)

The Hong Kong Polytechnic University

Jinzhong Xiang

Yunnan University

Rongbin Ji

Kunming Institute of Physics

Shu Ping Lau

The Hong Kong Polytechnic University

Kar Teng

Swansea University

Wei Guo

Beijing Institute of Technology

Yugui Yao

Beijing Institute of Technology <https://orcid.org/0000-0003-3544-3787>

Lain-Jong Li

University of New South Wales

Article

Keywords: Bi₂O₂Te films, two-dimensional (2D) materials

Posted Date: March 16th, 2021

DOI: <https://doi.org/10.21203/rs.3.rs-294003/v1>

License: © ⓘ This work is licensed under a Creative Commons Attribution 4.0 International License.

[Read Full License](#)

Ultrasensitive broadband photodetectors based on two-dimensional Bi₂O₂Te films

Pin Tian^{1,2}, Hongbo Wu³, Libin Tang^{1,2}✉, Jinzhong Xiang^{2,4}, Rongbin Ji¹, Shu Ping Lau⁵, Kar Seng Teng⁶, Wei Guo³, Yugui Yao³ and Lain-Jong Li⁷

Two-dimensional (2D) materials exhibit many unique optical and electronic properties that are highly desirable for application in optoelectronics. Here, we report the study of photodetector based on 2D Bi₂O₂Te grown on n-Si substrate. The 2D Bi₂O₂Te material was transformed from sputtered Bi₂Te₃ ultrathin film after rapid annealing at 400 °C for 10 min in air atmosphere. The photodetector was capable of detecting a broad wavelength from 210 nm to 2.4 μm with excellent responsivity of up to 3×10⁵ and 2×10⁴ AW⁻¹, and detectivity of 4×10¹⁵ and 2×10¹⁴ Jones at deep ultraviolet (UV) and short-wave infrared (SWIR) under weak light illumination, respectively. The effectiveness of 2D materials in weak light detection was investigated by analysis of the photocurrent density contribution. Importantly, the facile growth process with low annealing temperature would allow direct large-scale integration of the 2D Bi₂O₂Te materials with complementary metal-oxide–semiconductor (CMOS) technology.

¹Kunming Institute of Physics, Kunming 650223, P.R. China. ²Yunnan Key Laboratory of Advanced Photoelectric Materials & Devices, Kunming 650223, P.R. China. ³Beijing Key Laboratory of Nanophotonics and Ultrafine Optoelectronic Systems and Micro-nano Centre, School of Physics, Beijing Institute of Technology, Beijing 100081, China. ⁴School of Physics and Astronomy, Yunnan University, Kunming 650091, P.R. China. ⁵Department of Applied Physics, The Hong Kong Polytechnic University, Hong Kong SAP, P.R. China. ⁶College of Engineering, Swansea University, Bay Campus, Fabian Way, Swansea SA1 8EN, United Kingdom. ⁷School of Materials Science and Engineering, University of New South Wales, Sydney 2052, Australia. ✉email: scitang@163.com.

Since the discovery of graphene¹, there has been enormous interests in 2D materials, either layered²⁻⁶ or non-layered⁷⁻¹⁰, due to their fascinating and unique properties as compared to their bulk counterpart¹⁰⁻¹². Over the past decade, many 2D materials have found exciting applications in the field of optoelectronics, such as photocatalyses¹³⁻¹⁵, photodetectors¹⁶⁻¹⁸, solar cells^{19,20} and light-emitting diodes²¹⁻²³ (LEDs). Their extraordinary performances in optoelectronics are attributed to its high electron mobility, large specific surface area and energy band tunability. This has led to a significant increase in research activities on 2D materials in optoelectronics. Recently, Peng²⁴ et al synthesized a 2D Bi₂O₂Se material, which was different from traditional van der Waals 2D layered structure as its layers were held together by relatively weak electrostatic forces²⁵⁻²⁷. Importantly, the 2D Bi₂O₂Se nanoflakes prepared by chemical vapor deposition (CVD) method exhibited ultrahigh Hall mobility value of >20,000 cm²V⁻¹s⁻¹ and bandgap energy of ~0.8 eV that depended strongly on the film thickness due to quantum-confinement effects. This has led to an increasing research interests in the investigation of 2D bismuth oxychalcogenide (Bi₂O₂X; X = S, Se, Te) family. However, 2D Bi₂O₂Te, which is a cousin material of Bi₂O₂Se, consisting of a tetragonal structure with I4/mmm space group (a = 3.98 Å, c = 12.70 Å) of planar covalently bonded oxide layers (Bi₂O₂) sandwiched by Te square arrays with relatively weak electrostatic interactions (Fig. 1a), was

rarely investigated to date. The preparation of 2D Bi₂O₂Te material by CVD method remains a challenge due to the active characteristics of Te element, thus requires an extensive difference in the evaporation temperatures of Bi precursor and Te source during the growth process.

The different electronegativity²⁸ of Te (i.e., 2.10) and Se (i.e., 2.55) is very likely to endow Bi₂O₂Te with higher mobility and wider absorption spectrum than Bi₂O₂Se. In addition, the ease of oxidation of Te would allow 2D Bi₂O₂Te material to oxidize at much lower temperature during the preparation of dielectric layer. Such low temperature process is critical to the widespread application of 2D bismuth oxychalcogenide in the field of microelectronics.

While most 2D materials were synthesized using CVD method, the use of magnetron sputtering and rapid thermal annealing to prepare novel 2D Bi₂O₂Te materials at low temperature by transition from Bi₂Te₃ to Bi₂O₂Te under air atmosphere is reported herein. The technique is termed as rapid annealing phase transition (RAPT) method. In this work, a large-area 2D Bi₂O₂Te with excellent quality was prepared by the RAPT method. There has been much interest in integrating 2D materials with CMOS as demonstrated by Goossens et al²⁹. However, the high temperature needed for CVD growth and the difficulty in layer transfer of 2D materials on a wafer scale has hindered the immediate integration of 2D materials on CMOS. Thus, the low temperature growth method (e.g. below

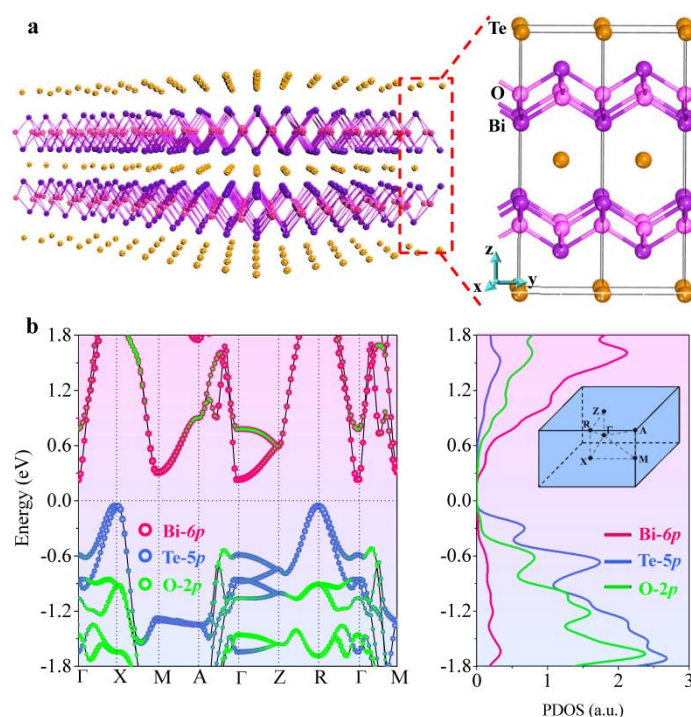


Fig. 1 Crystal structure and band-structure of bulk Bi₂O₂Te. **a** Bulk crystal structure (left) and side view (right) of the layer-dependent atomic structure of Bi₂O₂Te with space group I4/mmm (no. 139). **b** Band-structure (right panel) and the projected partial density of state (PDOS) of Bi₂O₂Te. Contributions of Bi-6p, Te-5p, and O-2p states are represented by pink, blue, and green circles, respectively. The Brillouin zone is shown as inset in right panel of (b). The Fermi level is shifted to zero.

tolerable CMOS process temperature of 400°C) can considerably simplify the integration process via direct growth of the 2D materials on CMOS platform. In this work, a photodetector based on the 400°C-grown 2D Bi₂O₂Te was fabricated and characterized. It responded to a broad wavelength range between 210 nm and 2.4 μm with high responsivity of up to 3×10⁵ and 2×10⁴ AW⁻¹, and detectivity of 4×10¹⁵ and 2×10¹⁴ Jones for ultraviolet (UV) and short-wave infrared (SWIR) respectively, which is extremely sensitive in weak light detection.

The ability of 2D materials in detecting weak light is still not well understood even though various 2D materials based photodetectors had been reported. By analyzing the contribution of photocurrent, the weak light detection capability is possibly attributed to the high separation efficiency of carriers generated in Bi₂O₂Te film.

Results and discussion

Compared to Bi₂O₂Se, the 2D Bi₂O₂Te exhibits a smaller bandgap of ~0.3 eV. Bulk Bi₂O₂Te calculations were performed at fixed experimental lattice constants. Fig. 1a shows the layer-dependent atomic structure of tetragonal Bi₂O₂Te verified by DFT calculations. As shown in Fig. 1b, the calculated band structure indicates that this system is an indirect narrow-gap semiconductor, with the valence band maximum (VBM) at X and the conduction band minimum (CBM) at Γ. From the projected density of states (PDOS), the low-energy electronic states close to Fermi level are primarily contributed by Bi-6*p* and Te-5*p* states with a small fraction of O-2*p* states. The VBM and CBM states are mainly originated from the Te 5*p*-orbital and Bi 6*p*-orbital bands, respectively. Notably, both CBM and VBM states at Γ and X possess sharp dispersions along Γ-X/Γ-M and X-Γ/X-M directions respectively, hence demonstrating strong in-plane interaction. The MBJ+SOC calculated

bandgap (Γ-X) is ~0.28 eV, which is slightly larger than HSE+SOC value of ~0.17 eV, and is in good agreement with the optical bandgap experiments and previous theoretical work^{30,31}. Besides, the variation of bandgap with the number of layers has been calculated theoretically (results are shown in Supplementary Fig. 1-2). The bandgap of 2D Bi₂O₂Te film gradually decreases with increasing film thickness, and reaches convergence at ~6 layers (e.g. thickness of ~40Å), which is consistent with experimental observations (details in Discussion 4). Fig. 2a depicts the growth process of 2D Bi₂O₂Te film from sputtered Bi₂Te₃ followed by rapid annealing under O₂ atmosphere (detailed parameters in Methods). A contagious film was diluted in alcohol and carried out by TEM, as shown in Fig. 2b. At the brink TEM image, an enlarged HRTEM image was observed and all kinds of lattice distance along different crystal orientation was measured and marked in Fig. 2c, which indicates the high quality crystal was prepared. More importantly, the HRTEM image can be furtherly amplified from violet area in Fig. 2d, and the top view crystal structure of Bi₂O₂Te along *c* axis (see in Fig. 2e) can perfectly nest into the HRTEM according to lattice space and white spot can be around with one Bi atom, one Te atom and two O atom under admission reasonable lattice distort due to extremal force, as displayed in Fig. 2d. For ensuring the atom ratio of Bi, O and Te is consistent with the stoichiometric Bi₂O₂Te, an accurate element analysis was carried out by STEM and mapping, as shown in Fig. 2f-i. And the EDS spectrum is shown in Supplementary Fig. 3c, and the elements ratio was listed in up-plane of Fig. 2f-i, which the impure elements Si and Cu respectively attribute to SiO₂ substrate and copper grid, and thus the atom ratio of Bi, O and Te is about 13.46%, 17.65% and 5.06%, the atom ratio of Bi₂O₂Te is close to chemical

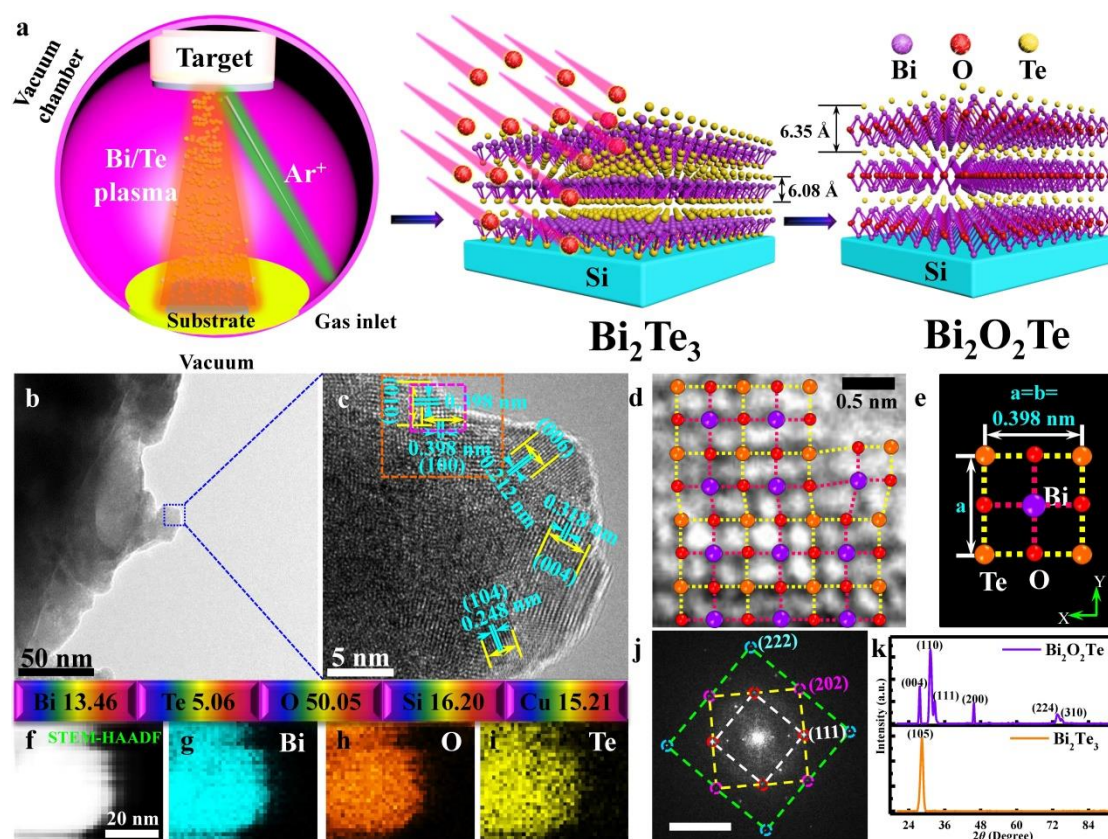


Fig. 2 Growth mechanism and characterization of 2D $\text{Bi}_2\text{O}_2\text{Te}$ prepared by RATP method. **a** Schematic illustration of the structural transformation from the sputtered Bi_2Te_3 to $\text{Bi}_2\text{O}_2\text{Te}$ film by rapid annealing. **b** The TEM image of $\text{Bi}_2\text{O}_2\text{Te}$. **c** High resolution transmission electron microscopy (HRTM) image of $\text{Bi}_2\text{O}_2\text{Te}$ enlarged from the blue rectangle area in left picture (**b**). **d** HRTEM image of $\text{Bi}_2\text{O}_2\text{Te}$ enlarged from violet rectangle area in HRTEM image (**c**), and the grid consisted of different color balls represent the structure of $\text{Bi}_2\text{O}_2\text{Te}$. **f-i**, Scanning transmission electron microscopy (STEM) image (**f**) of $\text{Bi}_2\text{O}_2\text{Te}$ and element mapping of Bi (**g**), O (**h**) and Te (**i**). The up-plane shows the ratio of various elements. **e** The crystal structure diagram of $\text{Bi}_2\text{O}_2\text{Te}$ along (001). **j** Fast Fourier transform (FFT) image, which indicates diffraction pattern of a square crystal structure, selected from TEM image of (**c**). **k** X-ray diffraction (XRD) pattern of Bi_2Te_3 and $\text{Bi}_2\text{O}_2\text{Te}$. Scale bars, 50 nm (**b**), 5 nm (**c**), 0.5 nm (**d**), 20 nm (**f**), 5 nm^{-1} (**j**).

stoichiometric 2:2:1. Besides, Fig. 2j shows the FFT image with distinctive diffraction pattern indicating crystallographic directions of (111), (202) and (222) (details in Supplementary Discussion 6). HRTEM images on the film, as shown in Supplementary Fig. 4a and b, exhibited high quality crystalline structure with crystal spacing of 0.281 nm along (110). The crystalline phase transition of the as-grown 2D materials was characterized using XRD (Fig. 2h). The Bi_2Te_3 has a strong peak at $2\theta = 28^\circ$, which was along (105). After rapid annealing, it experienced a phase transition to $\text{Bi}_2\text{O}_2\text{Te}$ exhibiting multiple peaks at $2\theta = 27.63^\circ, 31.21^\circ, 32.65^\circ, 45.71^\circ, 73.63^\circ, 75.07^\circ$, which were along (004), (110), (111), (200), (224) and (310), respectively (details in Supplementary Table 1). The polycrystalline structure of the 2D $\text{Bi}_2\text{O}_2\text{Te}$ film is shown in Fig. 2k, which consisted of numerous islands of crystal attributed to the polycrystalline structure of the Bi_2Te_3 precursor (Supplementary Fig. 5c-d and 6a-d). The XRD pattern in Fig. 2k is

consistent with the TEM and FFT images, which indicate high crystal quality of the $\text{Bi}_2\text{O}_2\text{Te}$ film.

The chemical bond in $\text{Bi}_2\text{O}_2\text{Te}$ was investigated using XPS. The XPS survey spectrum in Fig. 3a shows Bi, O and Te elements. The $\text{Bi}4f$ core level peak consisted of $\text{Bi}4f_{7/2}$ (158.2 eV) and $\text{Bi}4f_{5/2}$ (164.1 eV)³² (Fig. 3b). The $\text{O}1s$ core level peak was fitted with two components, namely Te-O-Bi (529 eV) and C-O (532.4 eV)^{33,34} (Fig. 3c). The core level peak of $\text{Te}3d$ was represented by $\text{Te}3d_{5/2}$ (575.8 eV) and $\text{Te}3d_{3/2}$ (586.2 eV)³⁵ (Fig. 3d). The XPS results indicated that the Bi, O and Te elements were chemically bonded instead of physically mixed. The 2D $\text{Bi}_2\text{O}_2\text{Te}$ film was characterized using TEM to study its crystal structure and morphology. Elemental mapping using EDX was performed on the as-grown $\text{Bi}_2\text{O}_2\text{Te}$ film to determine its stoichiometry as shown in Fig. 3e, f, i and j. Fig. 3g and h show the as-grown Bi_2Te_3 and $\text{Bi}_2\text{O}_2\text{Te}$ films having a thickness of 2.75 and 4 nm, respectively as measured using AFM. This suggests that the films

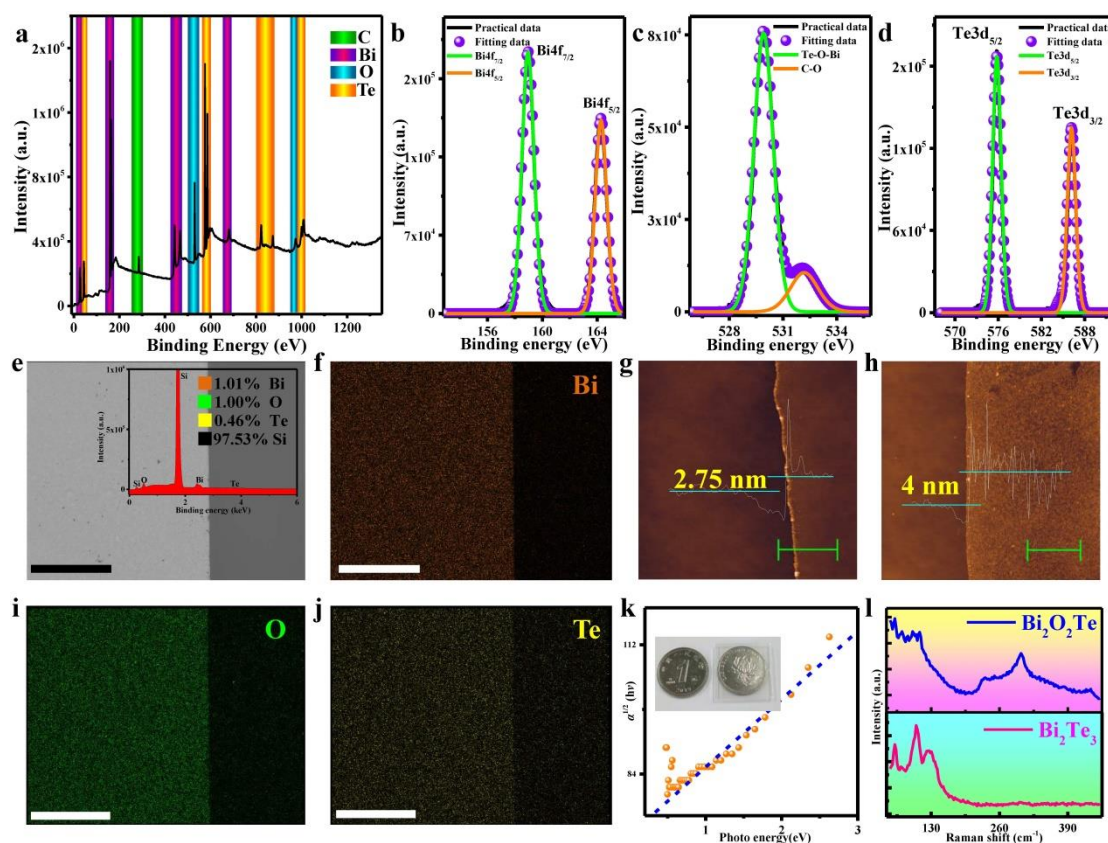


Fig. 3 Structural and morphology characterization of 2D $\text{Bi}_2\text{O}_2\text{Te}$. **a-d** X-ray photoelectron spectroscopy (XPS) of 2D $\text{Bi}_2\text{O}_2\text{Te}$ showing XPS survey spectrum on the film (**a**), spectra on core level of Bi4f (**b**), O1s (**c**) and Te3d (**d**). **e** Scanning electron microscopy (SEM) images of $\text{Bi}_2\text{O}_2\text{Te}$ film. **f, i** and **j** Elemental mapping of Bi, O and Te of 2D $\text{Bi}_2\text{O}_2\text{Te}$ grown on Si substrate, respectively. Inset of (**e**) shows the ratio of different elements calculated from energy dispersive spectroscopy (EDS) analysis. **g** and **h** Atomic force microscope (AFM) image of Bi_2Te_3 and $\text{Bi}_2\text{O}_2\text{Te}$ film, respectively. **k** Calculated optical bandgap of $\text{Bi}_2\text{O}_2\text{Te}$. Inset of (**k**) shows optical images of $\text{Bi}_2\text{O}_2\text{Te}$. **l** Raman spectrum of Bi_2Te_3 and $\text{Bi}_2\text{O}_2\text{Te}$. Scale bars, 200 μm (**e, f, i, j**), 5 μm (**g, h**).

consisted of 5–6 layers according to the interlayer distance of Bi_2Te_3 and $\text{Bi}_2\text{O}_2\text{Te}$ crystals (Fig. 2a), therefore demonstrating successful formation of the 2D materials. The thickness of the film can be controlled by sputtering duration as shown in Supplementary Fig. 7a–f. Besides, there was an obvious difference in optical properties between Bi_2Te_3 and $\text{Bi}_2\text{O}_2\text{Te}$ as shown in Supplementary Fig. 8a and Fig. 9a. The Bi_2Te_3 has an optical bandgap of ~ 0.14 eV (Supplementary Fig. 9b), which is in good agreement with previously reported works^{32,36–37}, while the measured bandgap of $\text{Bi}_2\text{O}_2\text{Te}$ was ~ 0.3 eV (Fig. 3k and details in Supplementary Discussion 5).

SEM image shows uniform coverage of the film on Si substrate and the film exhibited microstructure of 2D $\text{Bi}_2\text{O}_2\text{Te}$. Moreover, the size of the microstructure in 2D $\text{Bi}_2\text{O}_2\text{Te}$ would increase with sputtering duration of Bi_2Te_3 precursor (details in Supplementary Fig. 10a–d). The transition from Bi_2Te_3 to $\text{Bi}_2\text{O}_2\text{Te}$ can also be observed on Raman spectra as shown in Fig. 3l. The classical Raman shift of Bi_2Te_3 is shown in bottom panel of Fig. 3l,

which revealed four Raman peaks at 62.7, 93.4, 124.1 and 140.3 cm^{-1} corresponding to A_{1g}^1 , E_g^2 , A_{1u} , and A_{1g}^2 of Bi_2Te_3 ³⁸, respectively. As compared to Bi_2Te_3 , the Raman spectrum of $\text{Bi}_2\text{O}_2\text{Te}$ (top panel of Fig. 3l) shows several new peaks at higher wavenumber, such as 300.7 cm^{-1} (B_{1g}) and 433.6 cm^{-1} (E_g^2)³¹, while those peaks at low wavenumber have become vague.

A photodetector composed of Al, $\text{Bi}_2\text{O}_2\text{Te}$ and n-Si, as illustrated in Fig. 4a, was fabricated (details on fabrication process in Method). The rectification characteristics of photodetectors with different thickness of $\text{Bi}_2\text{O}_2\text{Te}$ film were investigated to determine the effect of film thickness on the built-in electric field at the device. It was found that the rectification behavior of the photodetector is worsen as the thickness of $\text{Bi}_2\text{O}_2\text{Te}$ film increases (details in Supplementary Fig. 11a). An optimal performance was observed in the photodetector with a $\text{Bi}_2\text{O}_2\text{Te}$ thickness of 4 nm (e.g. sputtering duration of 1 s). Under weak light illumination, there was an increase in current density of the photodetector, hence indicating the generation of photocurrent as

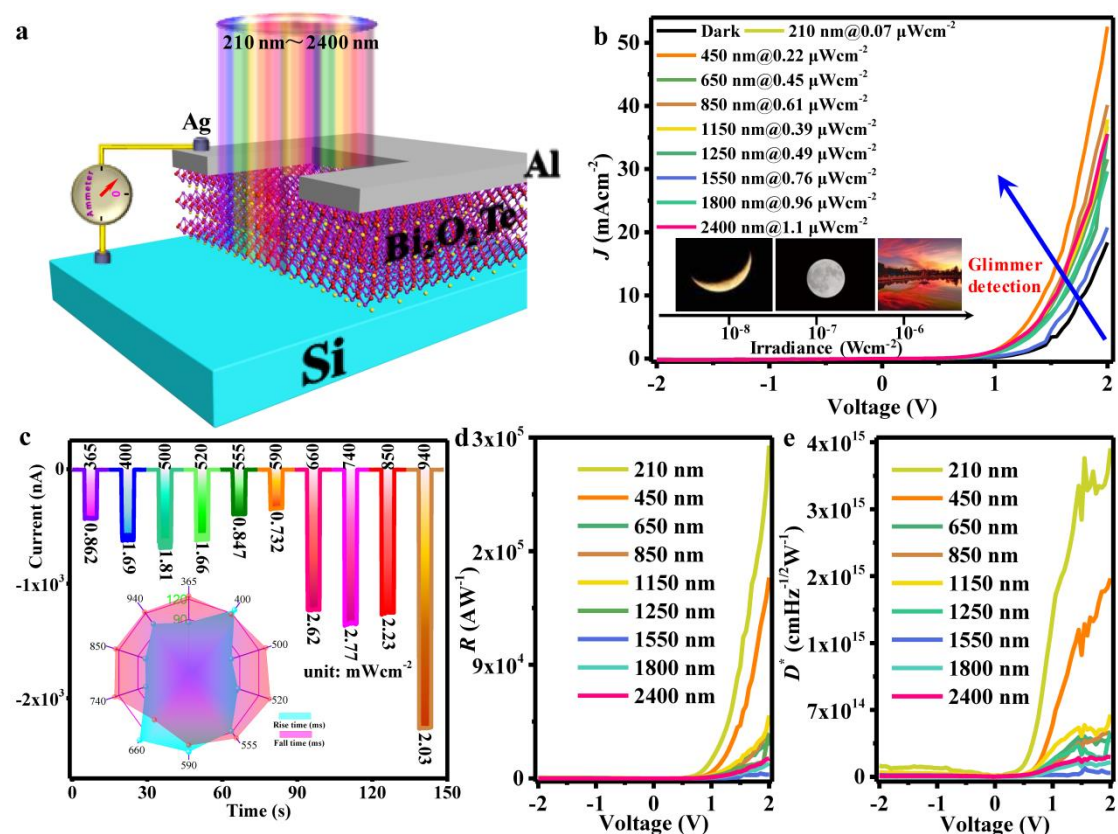


Fig. 4 Characterization of photodetector based on 2D $\text{Bi}_2\text{O}_2\text{Te}$. **a** Schematic diagram showing the structure of photodetector, composed of 2D $\text{Bi}_2\text{O}_2\text{Te}$ and n-Si substrate, with an active area of 4 mm^2 and responding to a broad wavelength between 210 nm and $2.4 \mu\text{m}$. **b** I - V curves of the photodetector in dark and under weak light illumination at different wavelengths. Inset pictures illustrate the variation of light power density for crescent, plenilune and sunset rang from nanowatt (nW) to microwatt (μW). **c** Transient response of photodetector at -2V applied voltage under LEDs illumination with various wavelengths at milliwatt power density (mWcm^{-2}). The inset diagram depicts the response time, which shows most rise time was shorter than fall time. **d** and **e** Responsivity and detectivity against voltage curves at different wavelengths under weak light illumination, respectively.

shown in Fig. 4b and Supplementary Fig. 11b. In addition, strong light source from LEDs was incident on the photodetectors, which exhibited similar photovoltaic effect as shown in Supplementary Fig. 12a and b. Transient response of the photodetector was measured under LEDs illumination at a range from 365 to 940 nm. The photodetector displayed stable and fast response with rise and fall time of 77.63 and 126.73 ms at 740 nm, respectively (as shown in Fig. 4c and Supplementary Fig. 13a-j). The rise and fall time under different incident light wavelengths was plotted in inset of Fig. 4c. Figures of merit, such as responsivity and detectivity, are often used to determine and compare the performance of photodetectors. For instance, responsivity can be expressed using the equation³⁹:

$$R = J_{\text{ph}} / P_{\text{opt}}$$

where J_{ph} is photocurrent that equals to the absolute value of the current density under illumination subtracting that in the dark, and P_{opt} is incident

optical power. Detectivity (D^*) can be expressed using the equation³⁹:

$$D^* = R / \sqrt{2q |J_{\text{dark}}|}$$

where J_{dark} is dark current density and q is unit charge. Both R and D^* can be calculated from the I - V characteristic curves. As shown in Fig. 4d and e, the photodetector exhibited excellent performance demonstrating detectable wavelength from 210 nm to $2.4 \mu\text{m}$ with responsivity of up to 3×10^5 and $2 \times 10^4 \text{ AW}^{-1}$, and detectivity of 4×10^{15} and 2×10^{14} Jones at deep ultraviolet (UV) and short-wave infrared (SWIR) under weak light illumination, respectively. To the best of our knowledge, the performance of the photodetector is superior than the state-of-the-art photodetectors based on 2D materials hybrid Si and outperformed those photodetectors based on 2D materials hybrid with Si as depicted in Supplementary Fig. 15a-d. The performance of the photodetector under strong light illumination using LEDs was also investigated (as shown in Supplementary Fig. 12c and d). However,

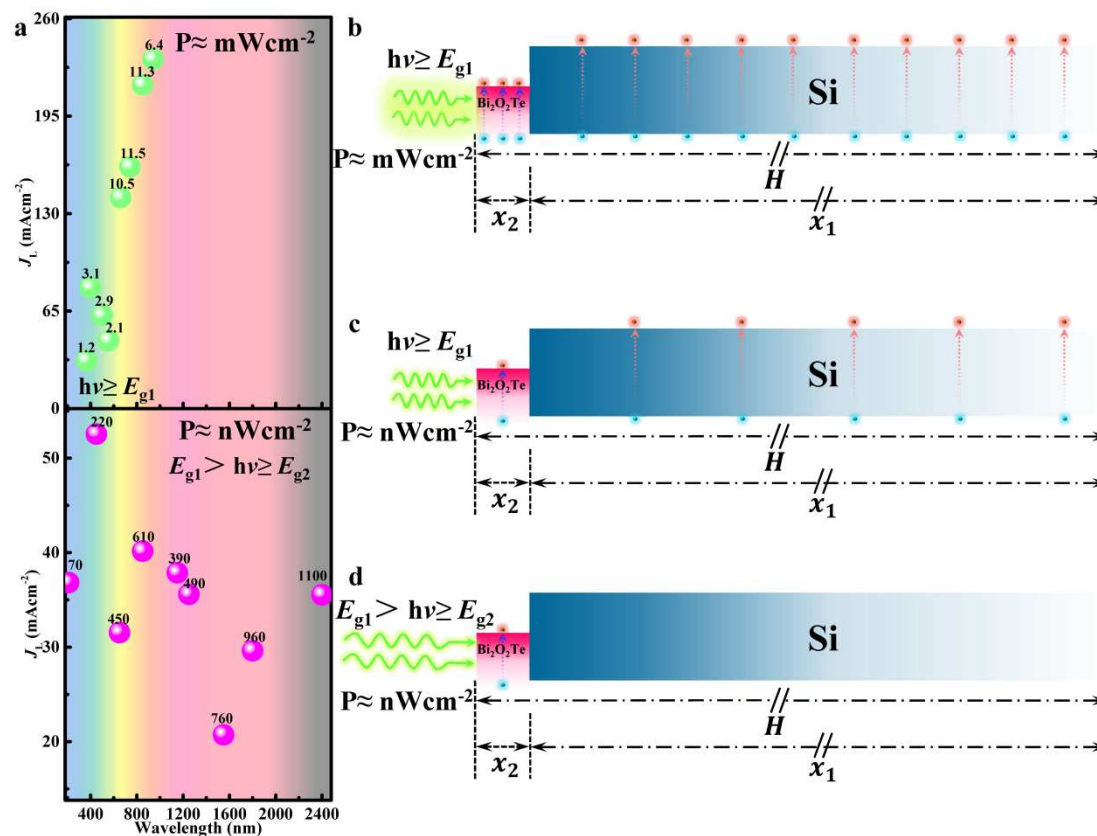


Fig. 5 Light current density contribution analysis. **a** The light current density (J_L) spectrum of photodetector with applied voltage of 2V under illumination of strong light source at milliwatt level (top) and weak light source at nanowatt level (bottom). **b-d** Photoelectric transport mechanism under different power irradiation of light sources with different wavelengths. Strong light with energy $h\nu \geq E_{g1}$ (bandgap of Si) incident on the device and both sides (Bi₂O₂Te and Si) generate abundant excitons (**b**). Weak light with energy $h\nu \geq E_{g1}$, both sides generate excitons but the number of electron-holes pair is less than that of strong light due to a decrease in the number of photons (**c**). Weak light with $E_{g1} > h\nu \geq E_{g2}$, only one side with smaller bandgap (e.g. E_{g2} , bandgap of Bi₂O₂Te) can generate excitons due to a decrease in photons energy (**d**).

the photodetector under strong light illumination exhibited poor performance as compared to weak light illumination. The voltage and current noise spectra of the photodetector were studied and represented in Supplementary Fig.16 and Fig. 17b, respectively. Besides, relevant parameters of the photodetector were also calculated and plotted in Supplementary Fig. 17d. The performance evaluation of the 2D Bi₂O₂Te based photodetector under direct current (DC) as well as alternating current (AC) mode was discussed in Supplementary Discussion 8. Further investigation was carried out to understand the effect of light current density on the performance of the photodetector. The contribution of current density from incident light on the photodetector, which composed of Bi₂O₂Te and Si, was attributed mainly by two parts, such as Bi₂O₂Te side with smaller bandgap energy (E_{g2}) and Si side with wider bandgap energy (E_{g1}) in an ideal case. Given the thickness of device (H) includes thickness of Si (x_1) and Bi₂O₂Te (x_2), as shown in Fig. 5b, the light current density of the device can be expressed as follow:

$$J_L = \int_0^\infty \int_0^H q G_L(x) dx d\lambda$$

where, J_L is light current density, q is unit charge, H is thickness of device, and $G_L(x)$ is rate of generation of photocarriers at position x . The $G_L(x)$ can be expressed using the equation:

$$G_L(x) = N_{\text{ph}}(\lambda) \beta [1 - R(\lambda)] \alpha(\lambda) e^{-\alpha(\lambda)x}$$

where $N_{\text{ph}}(\lambda)$ is number of photons with specific wavelength (λ) incident on device, β is probability of a photon producing a pair of photocarriers (e.g. $\beta=1$ if photon energy ($h\nu$) is larger than bandgap of semiconductor, otherwise $\beta=0$), $R(\lambda)$ is surface reflectance relative to wavelength, $\alpha(\lambda)$ is absorption coefficient of corresponding wavelength, and x is position of photocarriers. Since the photodetector was composed of different materials, which have different $R(\lambda)$, $\alpha(\lambda)$ and bandgap, the $G_L(x)$ can be divided into two parts, namely $G_L(x)_{\text{Si}}$ on the Si side and $G_L(x)_{\text{Bi}_2\text{O}_2\text{Te}}$ on the Bi₂O₂Te side, which can be expressed as:

$$G_L(x) = G_L(x)_{\text{Si}} + G_L(x)_{\text{Bi}_2\text{O}_2\text{Te}}$$

As the thickness of Si (400 μm) was much larger than that of Bi₂O₂Te (4 nm), the $G_L(x)$ is therefore

dominated by $G_L(x)_{Si}$ if the photon energy $h\nu \geq E_{g1}$ (Si bandgap). As shown in Fig. 5b and c, both $\text{Bi}_2\text{O}_2\text{Te}$ and Si sides would generate excitons but the number of excitons under weak light would be less than that of strong light due to a reduction in the photon number $N_{ph}(\lambda)$ of weak light. This inner mechanism is revealed in the light current density as shown in Fig. 5a. In the case of wavelength less than 1100 nm, which is the detection limit of Si, the light current density of weak light is distinctively smaller than that of strong light. However, in the case of $E_{g1} > h\nu \geq E_{g2}$, the β of Si is zero, so $G_L(x)_{Si} = 0$ and $G_L(x) = G_L(x)_{\text{Bi}_2\text{O}_2\text{Te}}$. Considering the saturation absorption characteristic of 2D materials due to the dominance of surface state⁴⁰, the strong light illuminated on 2D $\text{Bi}_2\text{O}_2\text{Te}$ would be ineffective as the ultrathin 2D materials do not fully convert all incoming photons into electron-hole pairs. As shown in bottom panel of Fig. 5a, the light current density of weak light illumination ($E_{g1} > h\nu \geq E_{g2}$) is of the same order as strong light ($h\nu \geq E_{g1}$) but the performance of the photodetector under weak light is much better than that of strong light (see Fig. 4c and d, and Supplementary Fig. 12c and d). Therefore, the 2D materials is more capable of detecting weak light, instead of strong light, than the bulk materials due to its surface state saturation absorption characteristics.

In this work, we have successfully developed a novel 2D $\text{Bi}_2\text{O}_2\text{Te}$ material with narrow bandgap prepared by a two-steps method, involving magnetron sputtering and rapid annealing. The 2D material was investigated by systematic theoretical calculations and multiple characterization techniques to confirm the transition of Bi_2Te_3 to $\text{Bi}_2\text{O}_2\text{Te}$ by rapid annealing under air atmosphere at 400 °C. A high performance photodetector, consisting of 2D $\text{Bi}_2\text{O}_2\text{Te}$ and Si heterojunction, was fabricated for weak light detection. Due to surface state saturation absorption characteristics of the 2D material, the device exhibited much better performance under weak light illumination than strong light. In summary, we have reported the growth of a novel 2D $\text{Bi}_2\text{O}_2\text{Te}$ material using the sputtering method, which is suitable for large-scale chip integration with CMOS technology. This 2D material has shown excellent performance as weak light photodetector with many potential applications.

Methods

Theoretical section

Structural optimization and band-structure calculations were performed based on density functional theory (DFT) as implemented in the Vienna ab-initio simulation package (VASP)^{41,42}. The projector-augmented-wave (PAW) method was utilized to describe the interactions between the ionic cores and the valence electrons^{43,44}. The Bi $6s^2 6p^3$, Te $5s^2 5p^4$ and O $2s^2 2p^4$ orbitals were explicitly included as valence electrons. The general gradient approximation of Perdew-Burke-Ernzerhof (PBE-GGA) was employed to treat the electronic exchange-correlation effects⁴⁵. Electronic wave functions were expanded using a plane wave basis set with an energy cutoff of 500 eV. The ionic relaxations were performed until the force on each atom was less than 0.01 eV Å⁻¹ and convergence criterion for the self-consistent electronic minimization loop was set to 10⁻⁵ eV. The Brillouin zone was sampled using a Monkhorst-Pack scheme during structure

relaxations⁴⁶. Due to the well-known underestimation of bandgap of PBE-GGA functional for semiconductors, the general gradient approximation-modified Becke-Johnson (GGA-MBJ)⁴⁷ method was adopted to compute the bandgap of bulk $\text{Bi}_2\text{O}_2\text{Te}$ with spin orbit coupling (SOC) effect included.

The 2D thin film of $\text{Bi}_2\text{O}_2\text{Te}$ structure was computed using a slab model. To keep the inversion symmetry of the bulk phase, both the top and bottom layers were terminated with Te atoms. To balance the non-stoichiometry due to the additional Te layers, hydrogen atoms were chosen to passivate the outermost Te layers. Similar structural treatment was adopted by Wu et al.²⁴. In vacuum, the electron density and kinetic energy density of MBJ method are close to zero, thus the MBJ calculations tend to diverse for 2D systems. To achieve high calculation accuracy, the hybrid Heyd-Scuseria-Ernzerhof (HSE) functional⁴⁸ was adopted for calculating the bandgap of $\text{Bi}_2\text{O}_2\text{Te}$ thin film. The HSE06+SOC bandgap calculations were too computationally expensive for large systems, thus we performed HSE06 bandgap calculations with SOC correction from differences between GGA+SOC vs GGA results. The thickness of vacuum layer was set to 15 Å to avoid periodic interactions. The van der Waals interaction was taken into account with the DFT-D3 method⁴⁹.

Preparation of 2D $\text{Bi}_2\text{O}_2\text{Te}$ and photodetector. A custom made magnetron sputtering technique (SPS-T-S100N-2G, Weinaworld) was used. Firstly, n-Si substrate, which has a resistivity of 1-10 Ω·cm and crystal orientation along <100>, was cleaned by acetone and ethanol. Next, the substrate was placed in a vacuum chamber (of <4.5x10⁻⁴ Pa) and heated at 200 °C in Ar (60scm) with working pressure kept at 5 Pa. The Bi_2Te_3 target (99.99%, purchased from ZhongNuoXinCai) was sputtered by radio frequency (RF) at 200 W for 1, 5, 10 and 15 s. Finally, the sputtered Bi_2Te_3 thin film was rapid annealed using RTP-1300 (ECOPIA) for 10 min at 400 °C with a rise time of 60 s under air atmosphere. A uniform, high quality $\text{Bi}_2\text{O}_2\text{Te}$ thin film on Si substrate was prepared. Photodetector was fabricated by depositing Al film on the 2D $\text{Bi}_2\text{O}_2\text{Te}$ thin film using a vacuum evaporation technique at pressure less than 6.9x10⁻⁴ Pa.

Characterization of $\text{Bi}_2\text{O}_2\text{Te}$ and Bi_2Te_3 film. Both Bi_2Te_3 and $\text{Bi}_2\text{O}_2\text{Te}$ thin films were characterized using Raman spectroscopy (XperRam Compact), XRD (EMPYREAN) UV-visible (U-4100) and TEM (Tecnai G2 TF30) techniques. The preparation process of $\text{Bi}_2\text{O}_2\text{Te}$ film for TEM measurement is as follows: firstly, a Si substrate was thinned to a few tens of micron using HF and sputtered with Bi_2Te_3 , and then oxidized to form $\text{Bi}_2\text{O}_2\text{Te}$. Next, the prepared sample was thinned further to remove the Si substrate using an ion milling equipment (691, Gantan). The Bi_2Te_3 film was etched from substrate through HF etching. Elementary composition of the samples was studied using XPS (K-Alpha⁺) with monochromated Al K α radiation. Uniformity and thickness of the film was measured using atomic force microscopy (AFM) (Seiko SPA-400) and field-emission scanning electron microscope (SEM, Quanta 200). The Fourier transform-infrared (FTIR) spectra of the Bi_2Te_3 film were acquired by Thermo Nicolet Avatar 360 spectrometer using attenuated total reflection (ATR). Hall measurement was carried out using Hall characterization system (HL5550 LN2 CRYOSTAT).

Characterization of photodetectors. $J-V$ measurements on the photodetector were performed using Keithley 2400 source meter. Strong light source was from LEDs with a variety of wavelengths (e.g. 365, 400, 500, 555, 660, 740 and 850 nm). Weak light source was obtained from deuterium lamp and bromine tungsten lamp (DSR-LSH-D30T75, Zolix) through spectrometer. The transient response measurement was performed using Keithley 2400 source meter with the LEDs driven by function/arbitrary waveform generator (RIGOL, DG 1022U). Besides, the power density of specific wavelength was measured by bolometer (FZ400, NBeT Group Corp.) and the power density spectra of the weak light was obtained by spectral responsivity measurement system (DSR100-D30T75) (see Supplementary Fig. 14). The spectra of voltage noise power density of the photodetector based on 2D $\text{Bi}_2\text{O}_2\text{Te}$ was carried out at 0 V by using a lock-in amplifier (HF2LI). All measurements were carried out at room temperature.

Data availability

The data that support the findings of this study are available from the first author upon request.

Received: xxxx; Accepted: xxxx;

Published: xx xx xxxx

References

- Novoselov, K. S. et al., Electric field effect in atomically thin carbon films. *Science* **306**, 666-669 (2004).
- Watts, M. C. et al. Production of phosphorene nanoribbons. *Nature* **568**, 216-220 (2019).
- Yang, J. et al. Formation of two-dimensional transition metal oxide nanosheets with nanoparticles as intermediates. *Nat. Mater.* **18**, 970-976 (2019).
- Fei, Z. et al. Two-dimensional itinerant ferromagnetism in atomically thin Fe_3GeTe_2 . *Nat. Mater.* **17**, 778-782 (2018).
- Lui, C. H., Liu, L., Mak, K. F., Flynn, G. W. & Heinz, T. F. Ultraflat graphene. *Nature* **462**, 339-341 (2009).
- Vlassiok, I. V. et al. Evolutionary selection growth of two-dimensional materials on polycrystalline substrates. *Nat. Mater.* **17**, 318-322 (2018).
- Wang, F. et al. Nanometre-thick single-crystalline nanosheets grown at the water-air interface. *Nat. Commun.* **7**, 10444, (2016).
- Wang, F. et al. 2D library beyond graphene and transition metal dichalcogenides: a focus on photodetection. *Chem. Soc. Rev.* **47**, 6296-6341 (2018).
- Liu, S. et al. Facile preparation of novel and active 2D nanosheets from non-layered and traditionally non-exfoliable earth-abundant materials. *J. Mater. Chem. A* **7**, 15411-15419 (2019).
- Zhu, C., Gao, D., Ding, J., Chao, D. & Wang, J. TMD-based highly efficient electrocatalysts developed by combined computational and experimental approaches. *Chem. Soc. Rev.* **47**, 4332-4356 (2018).
- Mounet, N. et al. Two-dimensional materials from high-throughput computational exfoliation of experimentally known compounds. *Nat. Nanotechnol.* **13**, 246-252 (2018).
- Zhou, J. et al. A library of atomically thin metal chalcogenides. *Nature* **556**, 355-359 (2018).
- Tan, C. et al. Recent advances in ultrathin two-dimensional nanomaterials. *Chem. Rev.* **117**, 6225-6331 (2017).
- Dhakshinamoorthy, A., Asiri, A. M. & Garcia, H. 2D metal-organic frameworks as multifunctional materials in heterogeneous catalysis and electro/photocatalysis. *Adv. Mater.* 1900617 (2019).
- Zhu, X. et al. Stabilizing black phosphorus nanosheets via edge-selective bonding of sacrificial C_{60} molecules. *Nat. Commun.* **9**, 4177 (2018).
- Lin, H. et al. Chalcogenide glass-on-graphene photonics. *Nat. Photon.* **12**, 798-805 (2017).
- Long, M. et al. Room temperature high-detectivity mid-infrared photodetectors based on black arsenic phosphorus. *Sci. Adv.* **3**, e1700589 (2017).
- Mak, K. F. & Shan, J. Photonics and optoelectronics of 2D semiconductor transition metal dichalcogenides. *Nat. Photon.* **10**, 216-226 (2016).
- Kato, T. et al. Transport of ions and electrons in nanostructured liquid crystals. *Nat. Rev.* **2**, 17001 (2017).
- Jariwala, D., Marks, T. J. & Hersam, M. C. Mixed-dimensional van der Waals heterostructures. *Nat. Mater.* **16**, 170-181 (2016).
- Withers, F. et al. Light-emitting diodes by band-structure engineering in van der Waals heterostructures. *Nat. Mater.* **14**, 301-306 (2015).
- Tsai, H. et al. Stable light-emitting diodes using phase-pure Ruddlesden-Popper layered perovskites. *Adv. Mater.* **30**, 1704217 (2018).
- Weidman, M. C., Goodman, A. J. & Tisdale, W. A. Colloidal halide perovskite nanoplatelets: an exciting new class of semiconductor nanomaterials. *Chem. Mater.* **29**, 5019-5030 (2017).
- Wu, J. et al. High electron mobility and quantum oscillations in non-encapsulated ultrathin semiconducting $\text{Bi}_2\text{O}_2\text{Se}$. *Nat. Nanotechnol.* **12**, 530-534 (2017).
- Fu, Q. et al. Ultrasensitive 2D $\text{Bi}_2\text{O}_2\text{Se}$ phototransistors on silicon substrates. *Adv. Mater.* **31**, 1804945 (2019).
- Luo, P. et al. PbSe quantum dots sensitized high-mobility $\text{Bi}_2\text{O}_2\text{Se}$ nanosheets for high-performance and broadband photodetection beyond 2 μm . *ACS Nano* **13**, 9028-9037 (2019).
- Liang, Y. et al. Molecular beam epitaxy and electronic structure of atomically thin oxyselenide films. *Adv. Mater.* 1901964 (2019).
- Xiao, J. et al. Anisotropic $\text{Bi}_2\text{O}_2\text{Se}(\text{Te})$ monolayer: realizing ultra-high carrier mobility and giant electric polarization in two-dimension. arXiv:1911.11327.
- Goossens, S. et al. Broadband image sensor array based on graphene-CMOS integration. *Nat. Photon.* **11**, 366-371 (2017).
- Wu, M., Zeng, X. C. Bismuth oxychalcogenides: a new class of ferroelectric/ferroelastic materials with ultra high mobility. *Nano Lett.* **17**, 6309-6314 (2017).
- Cheng, T. et al. Raman spectra and strain effects in bismuth oxychalcogenides. *J. Phys. Chem. C* **122**, 19970-19980 (2018).
- Liu, J. et al. Bi_2Te_3 photoconductive detectors on Si. *Appl. Phys. Lett.* **110**, 141109 (2017).
- Yashina, L. V. et al. Negligible surface reactivity of topological insulators Bi_2Se_3 and Bi_2Te_3 towards oxygen and water. *ACS Nano* **7**, 5181-5191 (2013).
- Bando, H. et al. The time-dependent process of oxidation of the surface of Bi_2Te_3 studied by x-ray photoelectron spectroscopy. *J. Phys.: Condens. Matter.* **12**, 5607-5616 (2000).
- Fu, J. et al. Bi_2Te_3 nanoplates and nanoflowers: synthesized by hydrothermal process and their enhanced thermoelectric properties. *Cryst. Eng. Comm.* **14**, 2159 (2012).
- Checkelsky, J. G., Ye, J., Onose, Y., Iwasa, Y. & Tokura, Y. Dirac-fermion-mediated ferromagnetism in a topological insulator. *Nat. Phys.* **8**, 729-733 (2012).
- Mu, X. et al. Enhanced electrical properties of stoichiometric $\text{Bi}_{10.5}\text{Sb}_{1.5}\text{Te}_3$ film with high-crystallinity via layer-by-layer in-situ growth. *Nano Energy* **33**, 55-64 (2017).
- Hussain, N. et al. Ultrahigh room-temperature photoluminescence from few to single quintuple layer Bi_2Te_3 nanosheets. *Adv. Opt. Mater.* **6**, 1701322 (2018).
- Gong, X. et al. High-detectivity polymer photodetectors with spectral response from 300 nm to 1450 nm. *Science* **325**, 1665-1667 (2009).
- Xu, J. L. et al. Ultrasensitive nonlinear absorption response of large-size topological insulator and application in low-threshold bulk pulsed lasers. *Sci. Rep.* **5**, 14856 (2015).
- Kresse, G. & Furthmüller, J. Efficiency of ab-initio total energy calculations for metals and semiconductors using a plane-wave basis set. *Comput. Mater. Sci.* **6**, 15-50 (1996).
- Kresse, G. & Furthmüller, J. Efficient iterative schemes for ab initio total-energy calculations using a plane-wave basis set. *Phys. Rev. B* **54**, 11169 (1996).
- Blöchl, P. E. Projector augmented-wave method. *Phys. Rev. B* **50**, 17953 (1994).
- Kresse, G. & Joubert, D. From ultrasoft pseudopotentials to the projector augmented-wave method. *Phys. Rev. B* **59**, 1758 (1999).
- Perdew, J. P., Burke, K. & Ernzerhof, M. Generalized gradient approximation made simple. *Phys. Rev. Lett.* **77**, 3865 (1996).
- Monkhorst, H. J. & Pack, J. D. Special points for Brillouin-zone integrations. *Phys. Rev. B* **13**, 5188 (1976).
- Tran, F. & Blaha, P. Accurate band gaps of semiconductors and insulators with a semilocal exchange-correlation potential. *Phys. Rev. Lett.* **102**, 226401 (2009).
- Heyd, J., Scuseria, G. E. & Ernzerhof, M. Hybrid functionals based on a screened Coulomb potential. *J. Chem. Phys.* **118**, 8207-8215 (2003).
- Grimme, S., Antony, J., Ehrlich, S. & Krieg, H. A consistent and accurate ab initio parametrization of density functional dispersion correction (DFT-D) for the 94 elements H-Pu. *J. Chem. Phys.* **132**, 154104 (2010).

Acknowledgements

This work was supported by National Natural Science Foundation of China (Grant Nos. 61106098, 51201150, 11374250 and 11864044), the Key Project of Applied Basic Research of Yunnan Province, China (Grant No. 2012FA003), and the Hong Kong Polytechnic University grant (1-ZVGH).

Author contributions

Pin Tian performed the growth of 2D Bi₂O₂Te and prepared the photodetector. Hongbo Wu carried out the theoretical calculation. Libin Tang, Shu Ping Lau, Kar Seng Teng, Wei Guo and Yugui Yao conceived the project. Libin Tang supervised this work. All authors participated in the discussion and contributed to the manuscript.

Competing interests

The authors declare no competing interests.

Additional information

Supplementary information is available for this paper at <https://doi.org/xxxx>.

Reprints and permissions information is available at www.nature.com/reprints.

Correspondence and requests for materials should be addressed to xx or xx.

Publisher's note: Springer Nature remains neutral with regard to jurisdictional claims in published maps and institutional affiliations.

© The Author(s), under exclusive licence to Springer Nature Limited xxxx

Figures

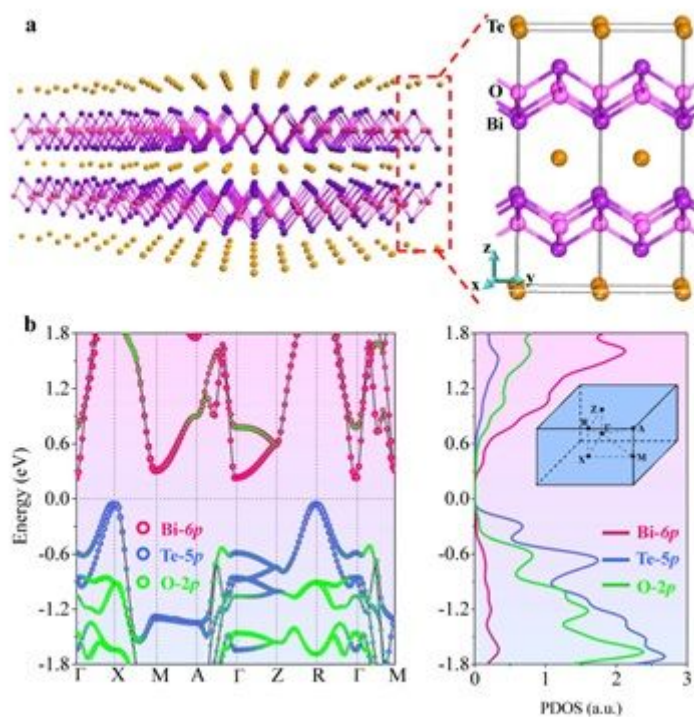


Figure 1

Crystal structure and band-structure of bulk Bi₂O₂Te. a Bulk crystal structure (left) and side view (right) of the layer-dependent atomic structure of Bi₂O₂Te with space group I4/mmm (no. 139). b Band-structure (right panel) and the projected partial density of state (PDOS) of Bi₂O₂Te. Contributions of Bi-6p, Te-5p, and O-2p states are represented by pink, blue, and green circles, respectively. The Brillouin zone is shown as inset in right panel of (b). The Fermi level is shifted to zero.

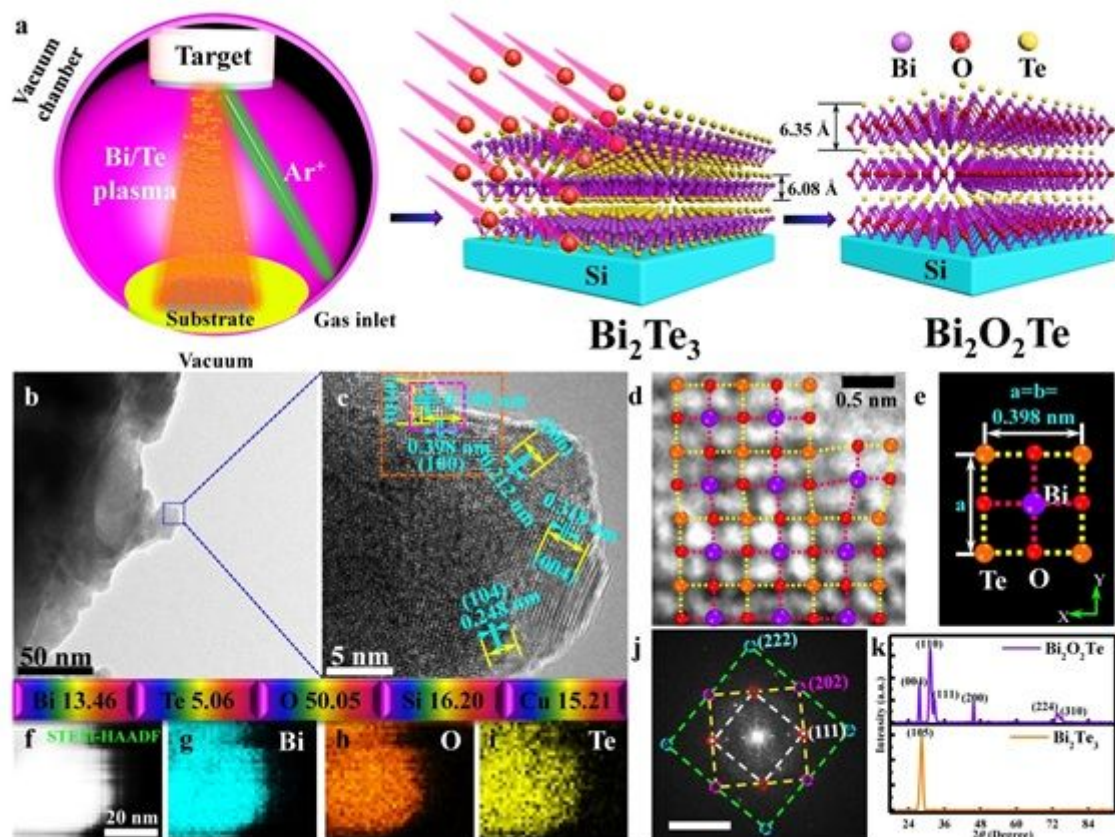


Figure 2

Growth mechanism and characterization of 2D Bi₂O₂Te prepared by RATP method. a Schematic illustration of the structural transformation from the sputtered Bi₂Te₃ to Bi₂O₂Te film by rapid annealing. b The TEM image of Bi₂O₂Te. c High resolution transmission electron microscopy (HRTEM) image of Bi₂O₂Te enlarged from the blue rectangle area in left picture (b). d HRTEM image of Bi₂O₂Te enlarged from violet rectangle area in HRTEM image (c), and the grid consisted of different color balls represent the structure of Bi₂O₂Te. f-i, Scanning transmission electron microscopy (STEM) image (f) of Bi₂O₂Te and element mapping of Bi (g), O (h) and Te (i). The up-plane shows the ratio of various elements. e The crystal structure diagram of Bi₂O₂Te along (001). j Fast Fourier transform (FFT) image, which indicates diffraction pattern of a square crystal structure, selected from TEM image of (c). k X-ray diffraction (XRD) pattern of Bi₂Te₃ and Bi₂O₂Te. Scale bars, 50 nm (b), 5 nm (c), 0.5 nm (d), 20 nm (f), 5 nm⁻¹ (j).

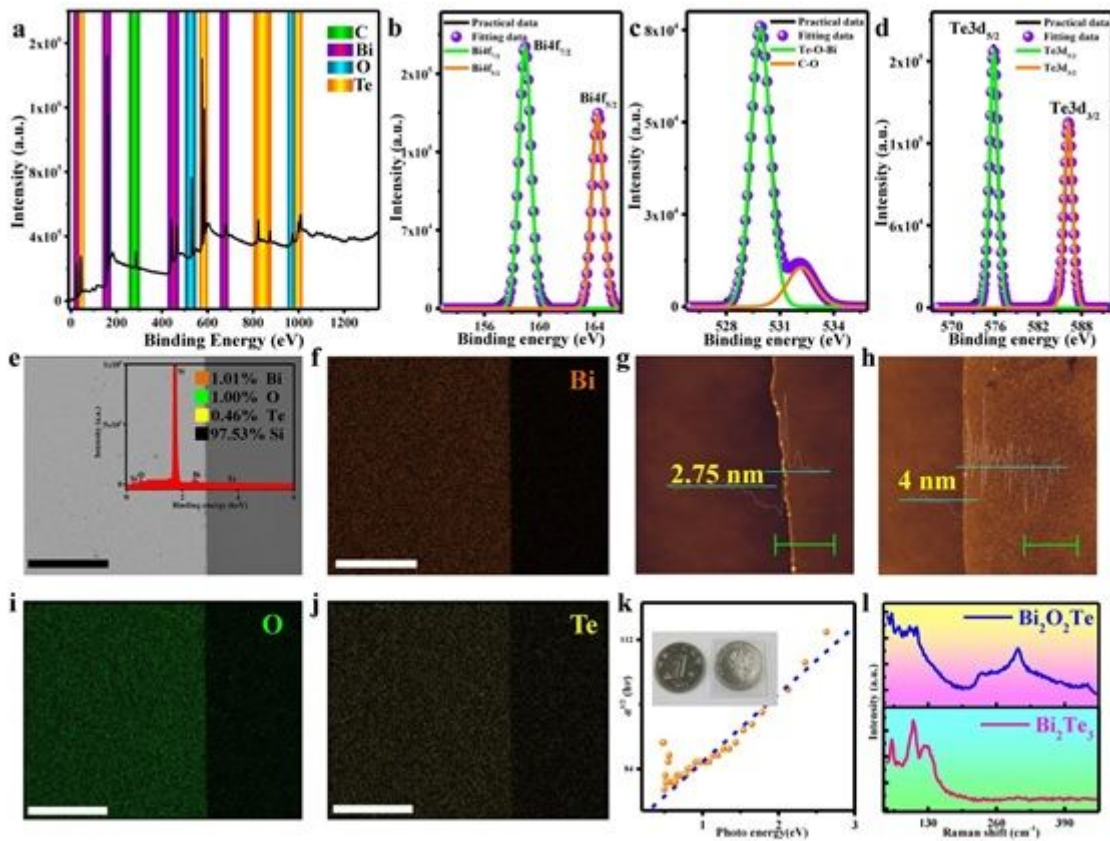


Figure 3

Structural and morphology characterization of 2D Bi₂O₂Te. a-d X-ray photoelectron spectroscopy (XPS) of 2D Bi₂O₂Te showing XPS survey spectrum on the film (a), spectra on core level of Bi4f (b), O1s (c) and Te3d (d). e Scanning electron microscopy (SEM) images of Bi₂O₂Te film. f, i and j Elemental mapping of Bi, O and Te of 2D Bi₂O₂Te grown on Si substrate, respectively. Inset of (e) shows the ratio of different elements calculated from energy disperse spectroscopy (EDS) analysis. g and h Atomic force microscope (AFM) image of Bi₂Te₃ and Bi₂O₂Te film, respectively. k Calculated optical bandgap of Bi₂O₂Te. Inset of (k) shows optical images of Bi₂O₂Te. l Raman spectrum of Bi₂Te₃ and Bi₂O₂Te. Scale bars, 200 μ m (e,f,i,j), 5 μ m (g,h).

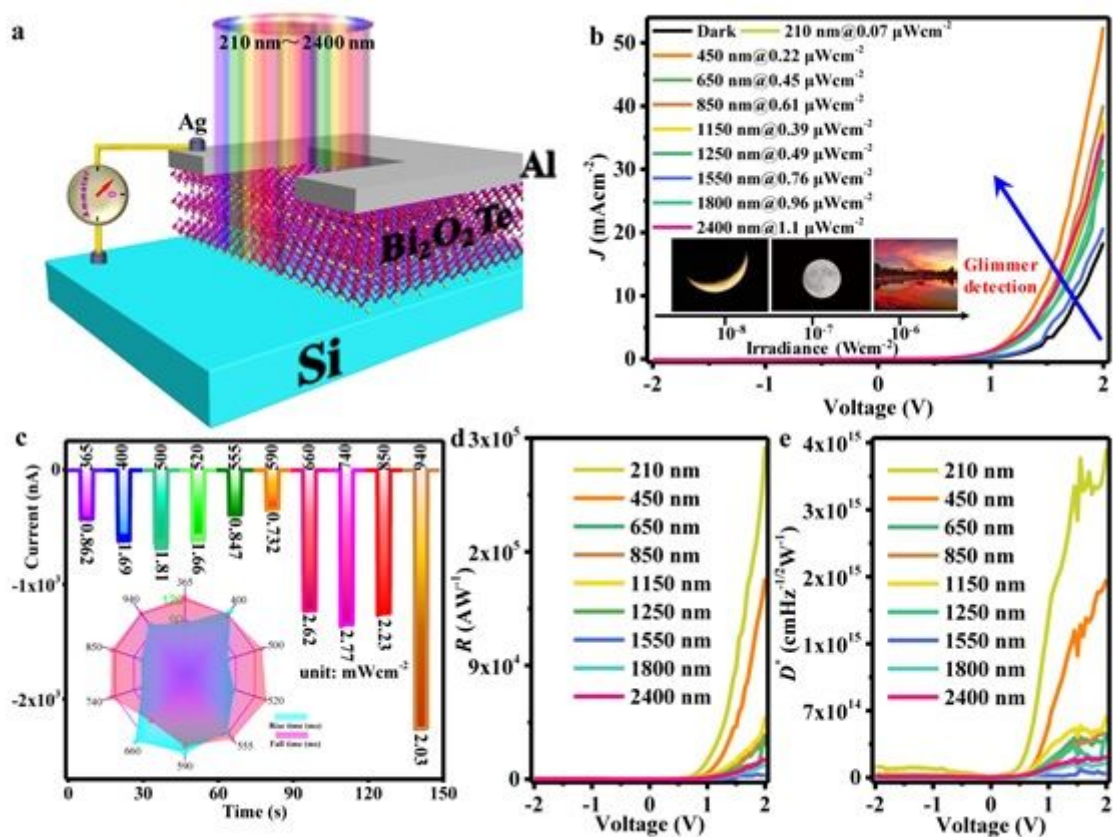


Figure 4

Characterization of photodetector based on 2D $\text{Bi}_2\text{O}_2\text{Te}$. a Schematic diagram showing the structure of photodetector, composed of 2D $\text{Bi}_2\text{O}_2\text{Te}$ and n-Si substrate, with an active area of 4 mm^2 and responding to a broad wavelength between 210 nm and $2.4 \mu\text{m}$. b I-V curves of the photodetector in dark and under weak light illumination at different wavelengths. Inset pictures illustrate the variation of light power density for crescent, plenilune and sunset rang from nanowatt (nW) to microwatt (μW). c Transient response of photodetector at -2V applied voltage under LEDs illumination with various wavelengths at milliwatt power density (mWcm^{-2}). The inset diagram depicts the response time, which shows most rise time was shorter than fall time. d and e Responsivity and detectivity against voltage curves at different wavelengths under weak light illumination, respectively.

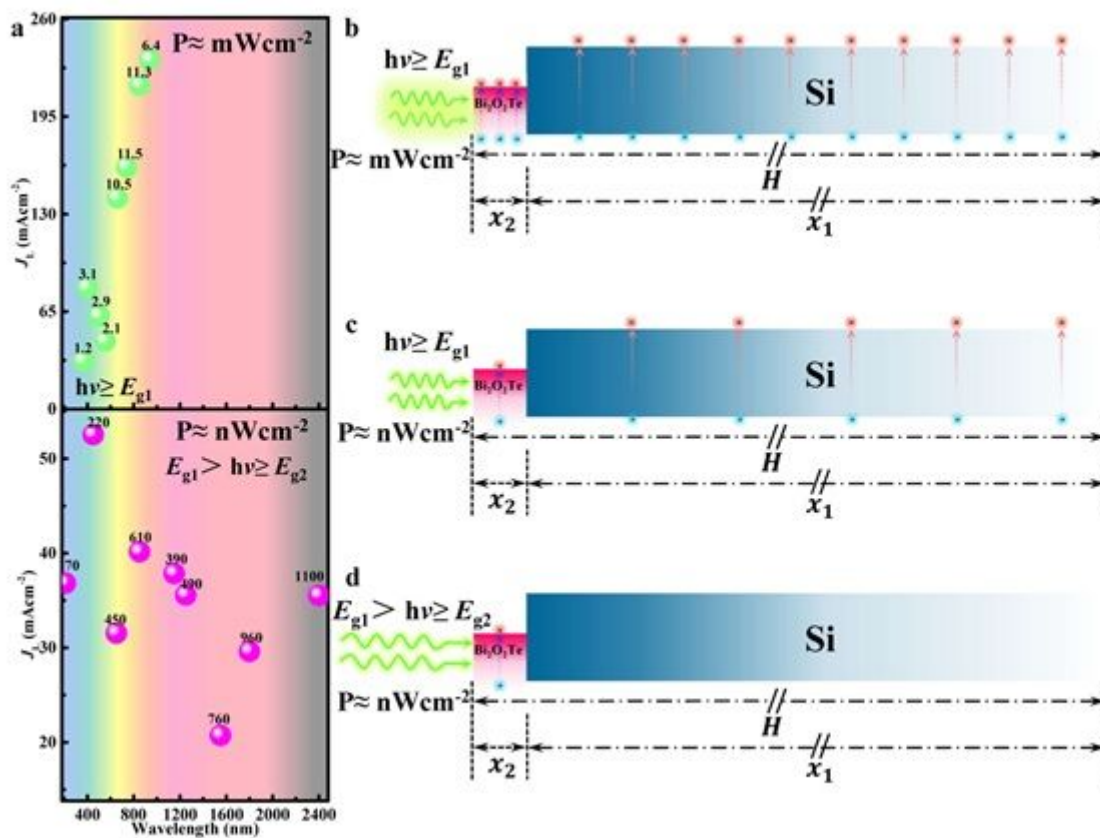


Figure 5

Light current density contribution analysis. a The light current density (J_L) spectrum of photodetector with applied voltage of 2V under illumination of strong light source at milliwatt level (top) and weak light source at nanowatt level (bottom). b-d Photoelectric transport mechanism under different power irradiation of light sources with different wavelengths. Strong light with energy $h\nu \geq E_{g1}$ (bandgap of Si) incident on the device and both sides (Bi₂O₃Te and Si) generate abundant excitons (b). Weak light with energy $h\nu \geq E_{g1}$, both sides generate excitons but the number of electron-holes pair is less than that of strong light due to a decrease in the number of photons (c). Weak light with $E_{g1} > h\nu \geq E_{g2}$, only one side with smaller bandgap (e.g. E_{g2} , bandgap of Bi₂O₃Te) can generate excitons due to a decrease in photons energy (d).

Supplementary Files

This is a list of supplementary files associated with this preprint. Click to download.

- [BOTSIXXXNCXXX.docx](#)